

Applications of Temporal Supersampling in Pulse-Burst PIV

Steven J. Beresh^{1,*}, Justin L. Wagner¹, Edward P. DeMauro¹,
John F. Henfling,¹ Russell W. Spillers,¹ and Paul A. Farias¹

1: Sandia National Laboratories, Albuquerque, NM, USA

* Correspondent author: sjberes@sandia.gov

Keywords: Time-resolved PIV, PIV processing, Turbulence

ABSTRACT

Time-resolved PIV has been accomplished in three high-speed flows using a pulse-burst laser: a supersonic jet exhausting into a transonic crossflow, a transonic flow over a rectangular cavity, and a shock-induced transient onset to cylinder vortex shedding. Temporal supersampling converts spatial information into temporal information by employing Taylor's frozen turbulence hypothesis along local streamlines, providing frequency content until about 150 kHz where the noise floor is reached. The spectra consistently reveal two regions exhibiting power-law dependence describing the turbulent decay. One is the well-known inertial subrange with a slope of $-5/3$ at high frequencies. The other displays a -1 power-law dependence for as much as a decade of mid-range frequencies lying between the inertial subrange and the integral length scale. The evidence for the -1 power law is most convincing in the jet-in-crossflow experiment, which is dominated by in-plane convection and the vector spatial resolution does not impose an additional frequency constraint. Data from the transonic cavity flow that are least likely to be subject to attenuation due to limited spatial resolution or out-of-plane motion exhibit the strongest agreement with the -1 and $-5/3$ power laws. The cylinder wake data also appear to show the -1 regime and the inertial subrange in the near-wake, but farther downstream the frozen-turbulence assumption may deteriorate as large-scale vortices interact with one another in the von Kármán vortex street.

1. Introduction

Technologies for time-resolved particle image velocimetry (TR-PIV) has evolved in low-speed flows using diode-pumped solid-state kHz-rate lasers and fast CMOS cameras, but the requirements of high-speed flows exceed the capabilities of these technologies. Instead, TR-PIV in high-speed flows is best accomplished using a pulse-burst laser, as this is the only light source capable of producing sufficient energy at the necessarily rapid pulse rates, though with the penalty of a very low duty cycle. Simultaneous with the maturation of pulse-burst laser technology, quality high-speed cameras have begun to achieve desirable framing rates without excessive sacrifice of the size of the spatial array. Pulse-burst PIV has a minimal history. Wernet appears to have been the first to achieve pulse-burst PIV [1], with more recent development offered by Brock et al [2] and Miller et al [3,4]. Pulse-burst PIV had not seen application in a

wind tunnel or other testing facility until Beresh et al demonstrated its use in a transonic wind tunnel [5].

However, even the 50 kHz repetition rate demonstrated thus far by pulse-burst PIV [5] is insufficient to capture the high frequencies associated with turbulent events in high-speed flows. This is doubly true when the Nyquist criterion is considered, halving the effective frequency response of a signal. Scarano and Moore [6] demonstrated an effective means of extracting considerably higher frequencies of information from TR-PIV than would be indicated merely by the framing rate of vector fields. In the time between successive velocity fields in a typical TR-PIV system, the flow convects by multiple vector spacings. The intervening vectors all contain valid information that may be introduced to the temporal signals. If Taylor's Hypothesis of frozen turbulence is valid over this short distance and time, the local instantaneous convection velocity may be used to convert these additional vectors to smaller time steps to fill the temporal gaps between actual data acquisition intervals. Scarano and Moore [6] describe such a supersampling algorithm and portray it as "pouring space into time." Fortunately, it is reasonable to employ Taylor's Hypothesis on these brief scales, even for small scales of turbulence. Crucially, the supersampling method employs local and instantaneous values for the convection velocity and direction rather than any averaged over time or space. Del Alamo and Jimenez [7] have shown this is necessary to yield an accurate representation of the turbulent energy spectra, which explains the success of Scarano and Moore's validation of the technique.

The supersampling technique of Scarano and Moore is not without limitations. Certainly, it cannot extract turbulent fluctuations at frequencies that exceed those of the particle response. Furthermore, the maximum frequency response is necessarily limited by the spatial resolution of a single vector measurement and by the time between laser pulse pairs. Another limitation is that planar PIV does not provide information on the out-of-plane convection and therefore supersampling must work solely with two-dimensional motion (even for stereoscopic PIV). In one of the test cases examined by Scarano and Moore, they discovered that the achievable supersampled frequency in a low-Reynolds-number jet was reduced due to nonlinear interactions in the large-scale vortices that dominated the flow. This motivated development of a more sophisticated algorithm by Schneiders et al [8] that incorporated solutions of the Navier-Stokes equations to avoid the assumptions of Taylor's Hypothesis. A related approach was demonstrated by Schreyer et al [9] that employed a dual PIV system with varying time delay between them, allowing reconstruction of spectral content but lacking the full spatio-temporal information of TR-PIV.

The present paper describes the application of temporal supersampling to examples in Sandia's high-speed test facilities. Previous publications have described the use of pulse-burst PIV in the Trisonic Wind Tunnel for a supersonic jet exhausting into a transonic crossflow [5, 10] and for transonic flow over a rectangular cavity [5, 11, 12]. In addition, pulse-burst PIV data have been acquired in the Multiphase Shock Tube for several applications including the transient onset of a von Kármán vortex street shed from a cylinder [13]. In each case, temporal phenomena were measured by the high repetition rates of pulse-burst PIV and are key to understanding the dominant physics describing the behavior of each of these flows. However, the turbulent behavior at all but the largest scales occurs at still higher frequencies. In the current work, these earlier data sets are reexamined by supersampling the existing data, potentially revealing turbulent properties not evident at the native framing rates of pulse-burst PIV.

2. Experimental Apparatus

Three distinct experiments are discussed in the present paper. These include two in Sandia's Trisonic Wind Tunnel (TWT) and one in Sandia's Multiphase Shock Tube (MST). A supersonic jet exhausting into a transonic crossflow was first described in [5] with expanded analysis in [10]. A preliminary data set for transonic flow over a rectangular cavity also was described in [5], then an improved and more comprehensive data set was detailed in [11, 12]; the latter data set is the cavity flow case studied herein. Finally, the shedding of a von Kármán vortex street from a cylinder was studied in the MST [13] and forms the final example of the current work. The hardware, instrumentation, and experimental approach are each briefly described in turn; fuller depictions may be found in the aforementioned publications.

2.1 Jet in Crossflow

Experiments were conducted in Sandia's Trisonic Wind Tunnel (TWT), which is a blowdown-to-atmosphere facility using air as the test gas. In its solid-wall transonic configuration, the test section is a rectangular duct of dimensions $305 \times 305 \text{ mm}^2$ ($12 \times 12 \text{ inch}^2$) and any Mach number between 0.5 and about 0.9 may be achieved by adjusting the area of a downstream throat. Mach 0.8 was tested exclusively for the data used herein with a stagnation pressure of 154 kPa and a fixed stagnation temperature of $321\text{K} \pm 2\text{K}$. The test section is enclosed within a pressurized plenum to accommodate ventilated test sections for other tunnel configurations.

The experiment was configured with a supersonic jet installed on the top wall of the transonic test section upstream of the windows, as seen in Fig. 1a. The upstream location of the jet

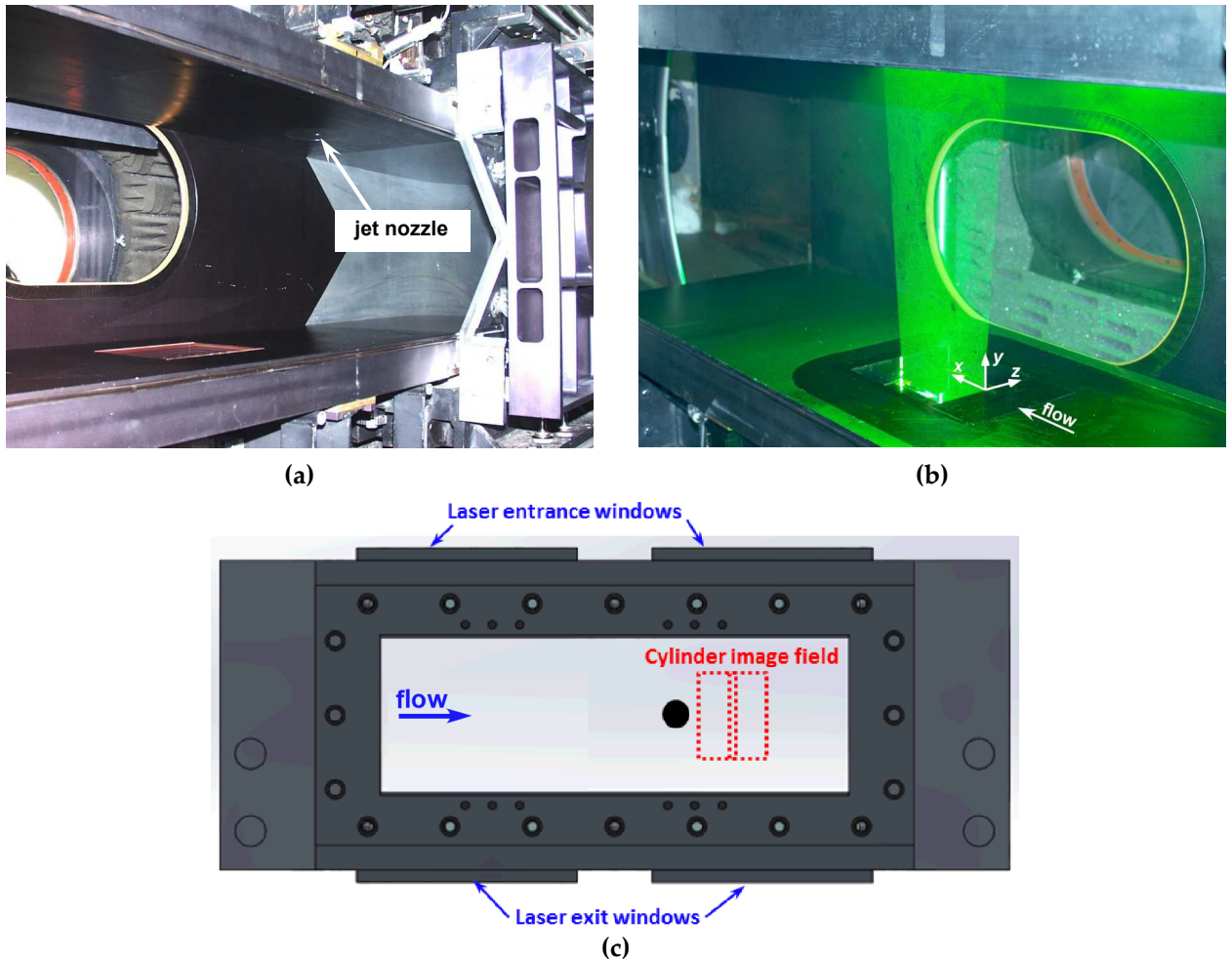


Fig. 1 Photo or sketch of the three experimental configurations. (a) The jet-in-crossflow experiment in the Trisonic Wind Tunnel. (b) The rectangular cavity flow in the Trisonic Wind Tunnel. (c) The cylinder wake experiment in the Multiphase Shock Tube.

positioned the imaging region for measurement of the far-field of the jet interaction once it has developed. The laser sheet was introduced through a window in the floor of the test section and was oriented in the streamwise center plane.

A nitrogen jet exhausted from a conical nozzle with a design Mach number of 3.73 and an exit diameter of 9.53 mm. The jet was operated at a pressure of 3.9 MPa to produce a jet-to-freestream dynamic pressure ratio of $J=8.1$. The coordinate axes originate at the centerpoint of the nozzle exit plane; the u component is in the streamwise direction and v component is positive away from the top wall of the tunnel.

The TWT is seeded by a thermal smoke generator (Corona Vi-Count 5000) whose output is

delivered to the TWT's stagnation chamber upstream of the flow conditioning section through a series of pipes and tubes, in which agglomeration of the particles occurs. Previous measurement of the in-situ particle response across a shock wave generated by a wedge showed the particle size to be 0.7 - 0.8 μm . Stokes numbers have been estimated as at most 0.05 based on a posteriori analysis of PIV measurements, which is sufficiently small to render particle lag errors negligible.

In the current work, a quasi-continuous burst-mode laser (QuasiModo-1000, Spectral Energies, LLC) with both diode- and flashlamp-pumped Nd:YAG amplifiers was used to produce a high-energy pulse train at 532 nm. The pulse-burst laser generates a burst of maximum duration 10.2 ms once every 8 seconds with a maximum repetition rate of 500 kHz. It produces 532-nm pulse energy of 500 mJ at its lowest repetition rate of 5 kHz and 20 mJ pulse energy at its highest repetition rate. The laser is capable of producing doublets with variable interpulse spacing at all repetition rates, which for the jet-in-crossflow experiment was $2.00 \mu\text{s} \pm 1 \text{ ns}$. In this work, 25 kHz doublets were used for PIV measurements with energy per pulse of 175 mJ for a 2.5 ms burst duration.

Images were acquired using two high-speed CMOS cameras (Photron SA-X2) which have a full framing rate of 12.5 kHz and an array of 1024×1024 pixels at this speed. Their windowing function allows the framing rate to be increased by sampling a semi-arbitrary portion of the imaging array. In the present case, each camera operated at 50 kHz with an array of 640×384 pixels. The two pulses in a doublet were frame-straddled around the cameras' interframe transfer time, which allowed cross-correlation analysis of pairs of images at 25 kHz. The cameras each were equipped with 200-mm focal length lenses. The two cameras were placed side by side to extend the field of view in the streamwise direction to track the convection of turbulent eddies, yielding a combined field of view of approximately $70 \times 21 \text{ mm}^2$ for two-component PIV.

A total of 53 bursts were acquired. Data were processed using LaVision's DaVis v8.2. In each case, image pairs were background corrected, intensity normalized, and then interrogated with an initial pass using 64×64 pixel interrogation windows, followed by two iterations of 24×24 pixel interrogation windows. A 50% overlap in the interrogation windows was used as well. The resulting vector fields were validated based upon signal-to-noise ratio, nearest-neighbor comparisons, and allowable velocity range.

2.2 Rectangular Cavity Flow

The cavity flow experiment also was conducted in TWT, but the test section was configured with porous walls on the top wall and one side wall to alleviate non-physical resonances due to wind tunnel duct modes [14]; a solid wall with a window for imaging was installed in the other side of the test section. Transonic data are given herein at Mach 0.80 with stagnation pressure 110 kPa and stagnation temperature $321\text{K} \pm 2\text{K}$. The TWT was seeded identically to the jet-in-crossflow experiments with equivalent Stokes number. The cavity is simply a rectangular pocket installed into the lower wall of the test section, having dimensions $127 \times 127 \text{ mm}^2$ with a nominal depth of 25.4 mm. A glass floor allowed the laser sheet to enter the cavity from below, as seen in Fig. 1b. The streamwise (x), wall-normal (y), and spanwise (z) coordinate system originated at the spanwise center of the cavity leading edge with y pointed away from the cavity.

In this case, the pulse-burst laser was configured to produce pulse pairs of separation $3.40 \mu\text{s} \pm 1 \text{ ns}$ at 37.5 kHz for bursts of 10.2 ms duration. About 27 mJ of energy was present in each pulse. The cameras were upgraded from the earlier experiments to Photron SA-Z's, which have a full framing rate of 20 kHz at 1024×1024 pixels but presently were operated at 75 kHz with an array of 640×360 pixels for frame-straddled acquisition of pulse pairs. Again, the two cameras were placed side by side to extend the field of view in the streamwise direction, yielding a combined field of view of $118 \times 31 \text{ mm}^2$ for two-component PIV. The cameras were angled downward by 12 deg to view about 55% into the depth of the cavity. This introduced a bias error in the vertical velocity component due to contamination by the out-of-plane component, estimated to reach as much as 20%; however, past experience has shown that this does not hinder visualization of the cavity flow or detection of turbulent eddies [15]. Scheimpflug mounts maintained focus despite the inclined view. Data were processed identically to that of the jet-in-crossflow experiment, though in this case 280 bursts were acquired.

2.3 Cylinder Wake

The Multiphase Shock Tube (MST) originally was constructed for studies of shock-induced dispersal of dense particle curtains [16]. In the present case, the MST was used as a conventional shock tube. The MST consists of a circular driver pipe having a diameter of 89 mm and a length of 2.1 m. The driven section is formed from square tubing having an inner width of 79 mm and length 5.2 m. The driven gas was ambient air at an initial temperature of about 300 K and an initial atmospheric pressure of about 84.1 kPa. For the present experiments, incident shock waves were generated by a fast-acting valve in place of the usual burst diaphragm. Schlieren and PIV measurements in the test section indicated the shock to be planar and core flow

conditions were identical to the burst diaphragm arrangement. The driver section was operated at 1380 kPa to produce a shock Mach number of 1.32.

The example flow in the shock tube detailed herein quantified the transient wake growth downstream of a cylinder following initiation by shock passage. Measurements were conducted in the wake of a cylinder of diameter 14 mm and spanning the entire width of the test section as sketched in Fig. 1c.

The pulse-burst laser is an ideal tool for use in a shock tube because the burst duration of 10.2 ms exceeds the total testing time of the facility while still producing large energies at high repetition rates. The laser was operated to produce pulse pairs at 50 kHz with energy of about 20 mJ per pulse in a 1.5-mm thick laser sheet, which was aligned parallel to the streamwise direction at the spanwise center of the test section.

Seed particles were produced using a TSI six-jet atomizer and entered the shock tube about 0.5 m downstream of the fast-acting valve through a remotely actuated solenoid and a duct having a diameter of 25 mm. An additional high-pressure solenoid and duct were installed at the end of the driven section and given a slight vacuum to distribute particles through the shock tube before operation of the shock tube. In-situ measurements across the incident shock gave a particle diameter of about 1.6 μm .

Two Photron SA-Z cameras, fitted with 100-mm focal length lenses, were placed on opposite sides of the test section to view adjacent image fields. The combined field-of-view was about 40 mm \times 35 mm mapped to a pixel resolution of 480 \times 340 for each camera, which were operated at 100 kHz to frame-straddle the 50 kHz doublets. Data were processed with the LaVision's Davis 8.2 to a final interrogation window of 24 \times 24 pixels (1.8 \times 1.8 mm²) at a 50% overlap. In this experiment, only 15 bursts of data were available for a single set of shock tube conditions.

3. Results and Discussion

3.1 Jet in Crossflow

A sample velocity field sequence for the supersonic jet in transonic crossflow is given in Fig. 2, showing four vector fields extracted from a much longer 2.5 ms burst duration at 25 kHz. Velocity fluctuations were found by calculating the mean velocity field over several wind tunnel runs and then subtracting it from each individual velocity field. The plot shows in-plane velocity fluctuations superposed on the derived vorticity field as a color contour and white

contour lines denoting the swirl field. The combined field-of-view of the high-speed cameras is situated far downstream of the jet exhaust and positioned to capture the turbulent eddies to be found at the windward mixing interface with the crossflow. The initial time in Fig. 2 is arbitrary within the longer burst duration.

Figure 2 illustrates one of the important characteristics of the entire data set. Counter-rotating pairs of eddies are found to repeat at regular intervals and convect downstream. Three pairs of eddies are seen at $t=0$, spaced across the field of view. The strongest pair is found near the downstream edge of the window and quickly convects out of the field in view in subsequent vector fields. A weaker pair of eddies is centered in the vector field and another situated near the upstream edge. In the final frame of Fig. 2, yet another pair of eddies enters the field of view. As these pairs convect downstream, the two eddies comprising a pair can be seen to rotate with respect to one another as they simultaneously drift farther out in the y direction, reflecting the gradual trajectory of the jet. Each of the eddies within a pair is separated by a reasonably consistent 8-10 mm and the distance between pairs is about 20-30 mm. These eddy separation distances are characteristic of the entire data set, as shown systematically in [10].

One of the most powerful contributions of pulse-burst PIV is the ability to measure velocity frequency spectra across an entire field of view. In the present case, however, the properties of the jet interaction change very little within the present field of view and it suffices to examine the spectra at two points. Figure 3 shows the power spectral density (PSD) at two points, one at the mean location of a turbulent eddy upstream and another downstream. Also included are data acquired at twice the acquisition rate, 50 kHz, by double-exposing particle images on a single frame and interrogating images using auto-correlations [5]. This is accomplished at a penalty of poorer spatial resolution and increased uncertainty, but is possible because there are no reverse velocities in the flow. Two PSD plots are shown, one for the streamwise component of velocity fluctuations and the other for the vertical component.

The PSD's of the streamwise component in Fig. 3a show approximately flat spectra prior to the rolloff at higher frequencies, but the vertical component PSD's in Fig. 3b display a distinct peak. The peaks of the power spectra in Fig. 3b reside at about 4 - 5 kHz with no appreciable difference between the upstream and downstream locations. The peak frequency roughly corresponds to a distance of 55 - 70 mm, using a convection velocity measured as $0.93\text{--}0.95 U_\infty$ by tracking the characteristic eddies. The separation between convecting pairs of vortices in movies such as Fig. 2 was found to be 25 - 30 mm, but these pairs tend to alternate whether they are led by a positively or negatively rotating vortex [10]. Therefore a full period – that is, the separation

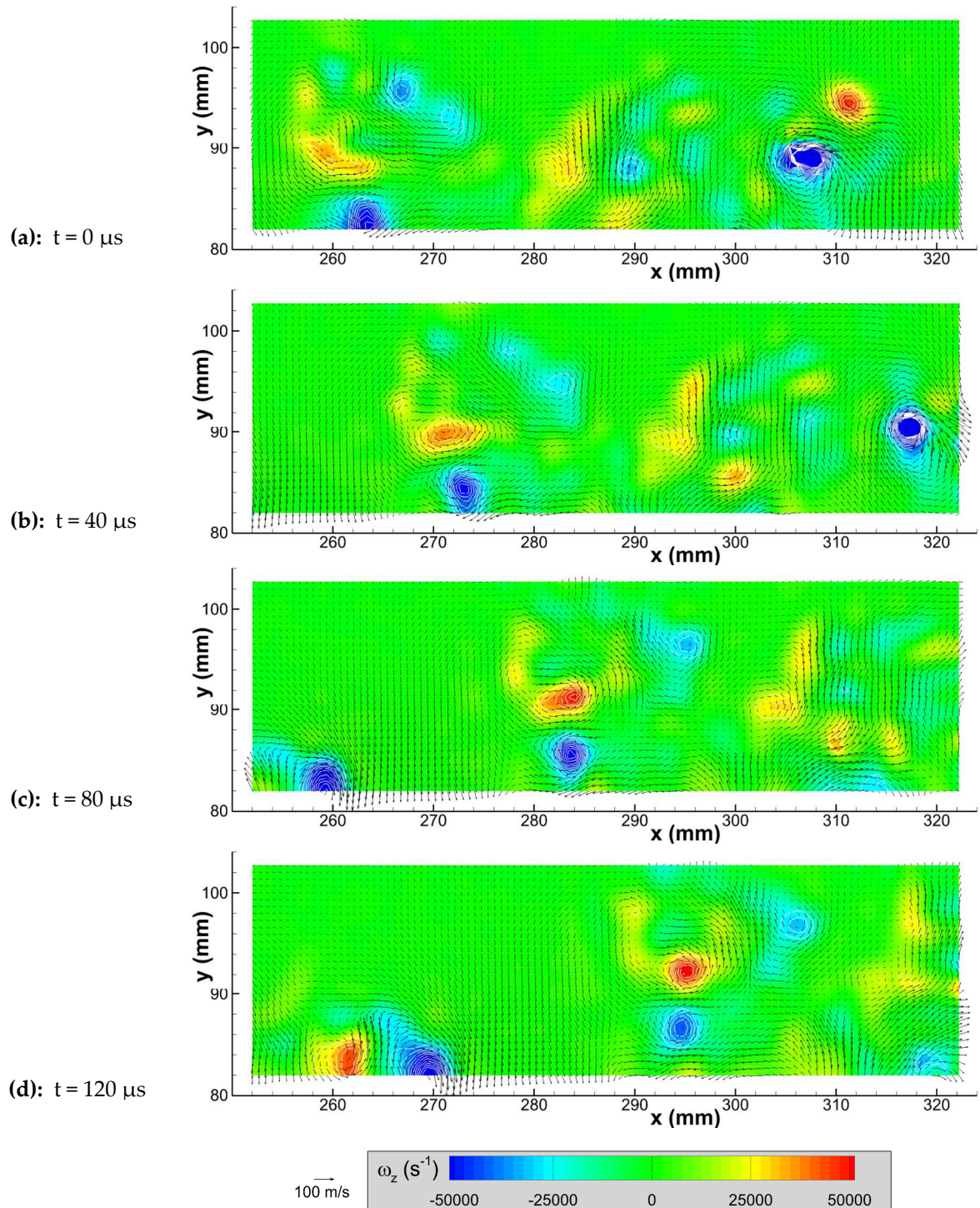


Fig. 2 Sequence of five velocity fields extracted from a 2.5 ms burst of 58 velocity fields for a Mach 3.7 jet issuing into a Mach 0.8 crossflow at $J=8.1$. Vectors show the in-plane velocity fluctuations superposed on a color contour plot of the derived vorticity field and white line contours of the swirl field.

between vortices of identical sign – is about 50 – 60 mm. This corresponds passably well to the peak frequency observed in the PSD's of Fig. 3b, suggesting that the tendency towards orderly passage of vortex pairs is identifiable in the frequency content of the flowfield.

Considerable additional quantitative information is available from the temporal aspect of the pulse-burst PIV data. The power spectra of Fig. 3 contain useful information at frequencies exceeding that of the peak in Fig. 3b and corresponding to spatial scales smaller than the large-scale vortices discussed to this point. At high frequencies, the correlation noise of the cross-correlated data becomes evident at about 8 kHz and appears to initiate a noise floor, whereas the higher-frequency noise in the auto-correlated data appears at about 15 kHz and continues a trend of diminishing energy as frequency rises. Aliasing may also be present at higher frequencies, artificially raising their magnitudes. It is well-known that the velocity power spectra should obey a power-law dependency of $-5/3$ once the inertial subrange of turbulence scales is reached (e.g., Pope [17]). However, in the present case this regime is unlikely to have been reached by the current temporal capability. A rough estimate based on Kolmogorov scaling indicates the expected onset of the $-5/3$ slope would be above 20 kHz; adapting the simulations of Kawai and Lele [18] suggests about 30 kHz.

Nonetheless, a uniform slope appears to exist from about 5 – 25 kHz in spectra of the vertical velocity component shown in Fig. 3b. This slope appears consistent with a -1 dependency, which is well established at frequencies lower than those of the inertial subrange in pressure power spectra beneath wall-bounded turbulence (e.g., Bull [19]) but its existence in the velocity field remains elusive [20-22]. Nickels et al [23] provide an excellent summary of why it is so difficult to detect in wall-bounded turbulence. It is unclear from Fig. 3b whether the present dependency has been located because the jet-in-crossflow physics produce it at lower Reynolds numbers than in wall-bounded turbulence or whether the manifestation of PIV correlation noise and aliasing effects have coincidentally generated an apparent -1 slope.

An answer to this ambiguity may be found in still higher frequencies contained within the pulse-burst PIV data. In the 40 μ s between successive velocity fields, the flow convects by about 16 vector spacings. The intervening 15 vectors all contain valid information that may be introduced to the temporal signals using temporal supersampling as described in the introduction of this paper. An algorithm similar to Scarano and Moore's [6] has been employed for the cross-correlated pulse-burst PIV; the auto-correlated data will yield inferior supersampled information because the interrogation windows are larger and the correlations noisier, leading to poorer vector quality between time steps. In addition, high-frequency noise was treated within the

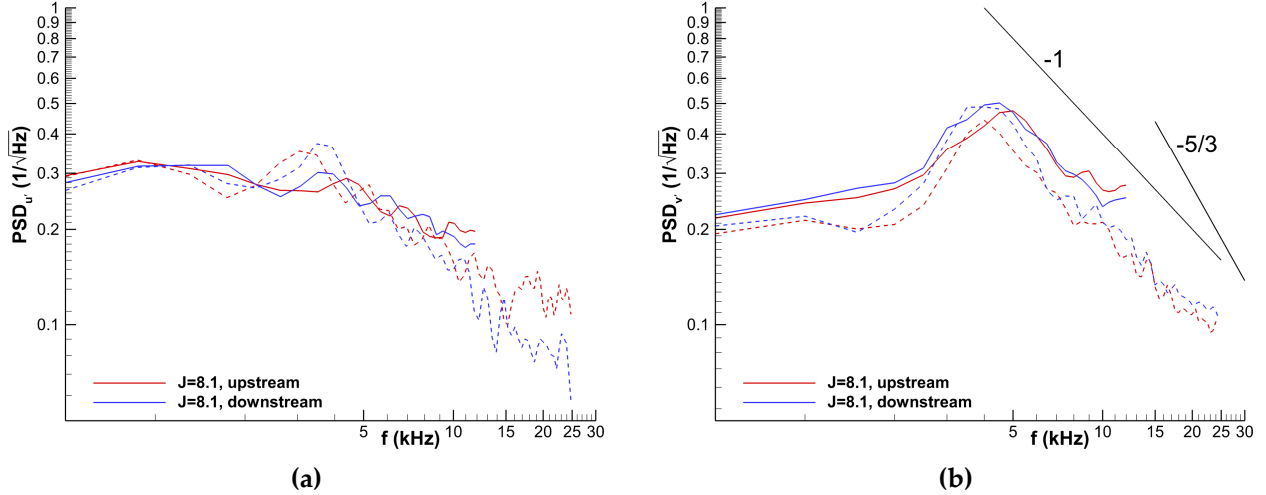


Fig. 3 Power spectra of velocity fluctuations for the jet in crossflow, measured at an upstream location in the field of view and a downstream location. Solid lines denote cross-correlation data at 25 kHz and broken lines are auto-correlation data at 50 kHz. (a) streamwise component; (b) vertical component.

DaVis software package using a second-order polynomial fit over 3×3 vector windows; no other vector smoothing was used in this case. A supersampling factor of 16 was used to reflect the number of vectors between successive vector fields, reducing the time between snapshots to $2.5 \mu\text{s}$, which still exceeds the frequency response limitation of the $2.0 \mu\text{s}$ time between paired laser pulses. Though out-of-plane motion cannot be accounted by the supersampling algorithm in a planar measurement, this flowfield is dominated by convective motion nearly aligned with the freestream direction. Out-of-plane velocity fluctuations are small as identified by a spanwise turbulence intensity less than 0.1.

The supersampled power spectra are shown in Fig. 4. Since no significant difference between the upstream and downstream locations was noted, only a single location is used in Fig. 4, with the supersampling acquired nearer to the center of the field of view where no edge effects interfere with following streamlines forward and backward to obtain convected vectors. The previous spectra from Fig. 3 are not shown superposed to allow a clear view of the new spectra, but they were found in good agreement with the supersampled data until their noise floor rose.

The most consequential of the supersampled spectra is the vertical component in Fig. 4b. The supersampled results well match the auto-correlated data to the end of their range, then continue the -1 slope dependence to about 40 kHz before gradually transitioning to an apparent $-5/3$ slope dependence. The noise floor begins to show at about 150 kHz, even with the

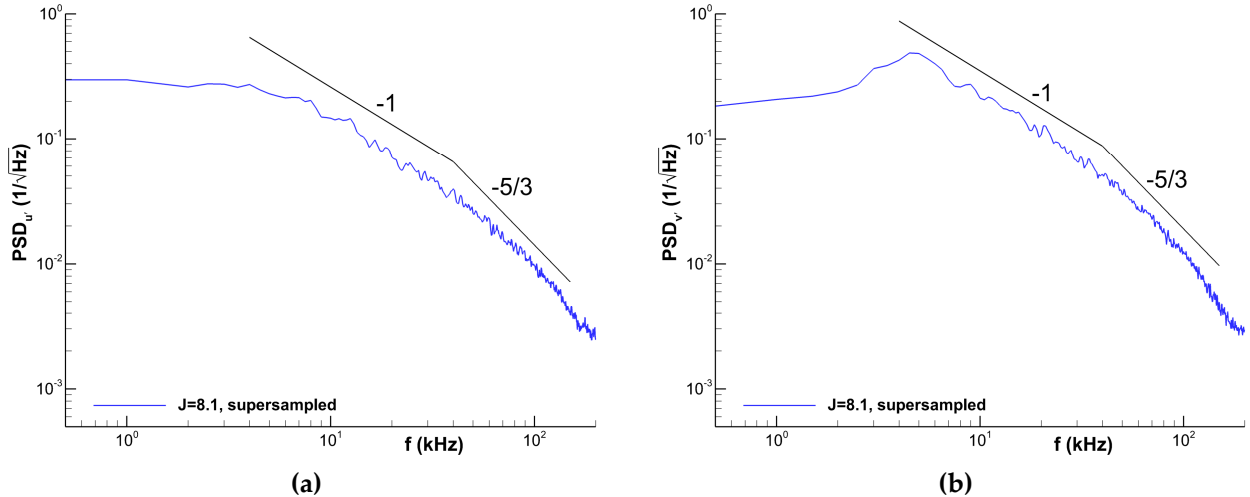


Fig. 4 Supersampled power spectra of velocity fluctuations for the jet in crossflow, measured near the center of the field of view. (a) streamwise component; (b) vertical component.

denoising algorithm that was employed. The presence of the $-5/3$ region, as remarked earlier, is well-known and expected as a consequence of the inertial subrange of turbulence decay. The -1 dependence, on the other hand, is an unanticipated discovery but appears to be substantiated by the supersampled data. Note that the denoising algorithm and any remaining aliasing effects would influence frequencies well into the $-5/3$ regime and not those of the -1 regime (several denoising algorithms were tested and had a demonstrable influence only for frequencies exceeding about 100 kHz). The -1 regime lasts for a full decade, from approximately 4 – 40 kHz. The streamwise component in Fig. 4a appears to be supportive of a -1 slope dependence as well but its lack of a peak means this region does not initiate until about 8 kHz. The $-5/3$ slope dependence at high frequencies is somewhat less convincing for the streamwise component than for the vertical component.

The vector spatial resolution is about 1.2 mm based simply on the size of the final interrogation window, which corresponds to a frequency of 220 kHz at the convection velocity. However, translating the interrogation window size into a frequency response limit is not straightforward due to its sensitivity to numerous details of the interrogation algorithm that couple with one another [24, 25]. Moreover, the modulation is gradual, typically a sinc function, rather than a definitive threshold [e.g., 25, 26]; therefore some loss of amplitude will occur over a range of frequencies near the cutoff. Nogueira et al [25] suggest that with 50% overlap or more between interrogation windows in multi-iteration analysis and a particle displacement not exceeding half the window size, the minimum detectable fluctuation wavelength is on the scale of the final

interrogation window. This indicates that the frequency cutoff due to the spatial resolution of a vector is indeed around 220 kHz and therefore adequate frequency response should be available to capture the inertial subrange in Fig. 4.

The -1 regime occurs at frequencies lying between the inertial subrange and the spacing of large-scale vortices of common sign, the latter of which has been seen to be a distance of about 50 – 60 mm. The inertial subrange appears to begin at about 40 kHz in Fig. 4b, which would correspond to a length scale of about 7 mm. Pope [17] suggests that the upper bound of the inertial subrange can be approximated as 1/6 of the integral length scale, whose value was calculated for the present conditions by Beresh et al [27] as about 40 mm. One-sixth of this is therefore 6.5 – 7 mm, in remarkable agreement with the estimate derived from Fig. 4b. This scale is roughly comparable to the smallest visually discernable vortices in the PIV vector fields of Fig. 2. This would seem to indicate that vortices on the scale of 7 – 60 mm are responsible for the behavior of the -1 regime, which would correspond to the dominant turbulent eddies observed by the present PIV measurements and matches Pope's description of an energy-containing subrange. Though experimental precedent is poor for the -1 power law in free shear flows, the supersampled PIV data have the necessary signal response to capture it and the resulting range of this spectral regime is consistent with turbulence theory.

3.2 Rectangular Cavity Flow

Given the success of temporal supersampling in detecting turbulent scaling laws in the jet-in-crossflow experiment, the same technique was turned to the rectangular cavity flow data. A sample pulse-burst PIV velocity field sequence is shown in Fig. 5, offering four snapshots extracted from a 10.2 ms burst of 386 velocity fields acquired at 37.5 kHz. Vectors show the in-plane velocity fluctuations superposed on a color contour plot of the streamwise velocity component; white line contours portray the vorticity magnitude exceeding a minimum threshold to emphasize the strongest regions of shear and turbulent eddies. In each figure, the positions of the cavity walls coincide with the axes and are shaded gray. The initial time is arbitrary, set to the first vector field in the burst.

Figure 5 shows a sequence of velocity fields leading to a strong ejection event at the aft end of the cavity. A large upswell is visible near the center of the first snapshot. As it approaches the aft end, it draws in fluid from the recirculation region, strengthening the ejection event. A more complete description of the cavity dynamics is found in [11] and discusses how motion within the recirculation region and the shear layer may interact to create a large-scale turbulent

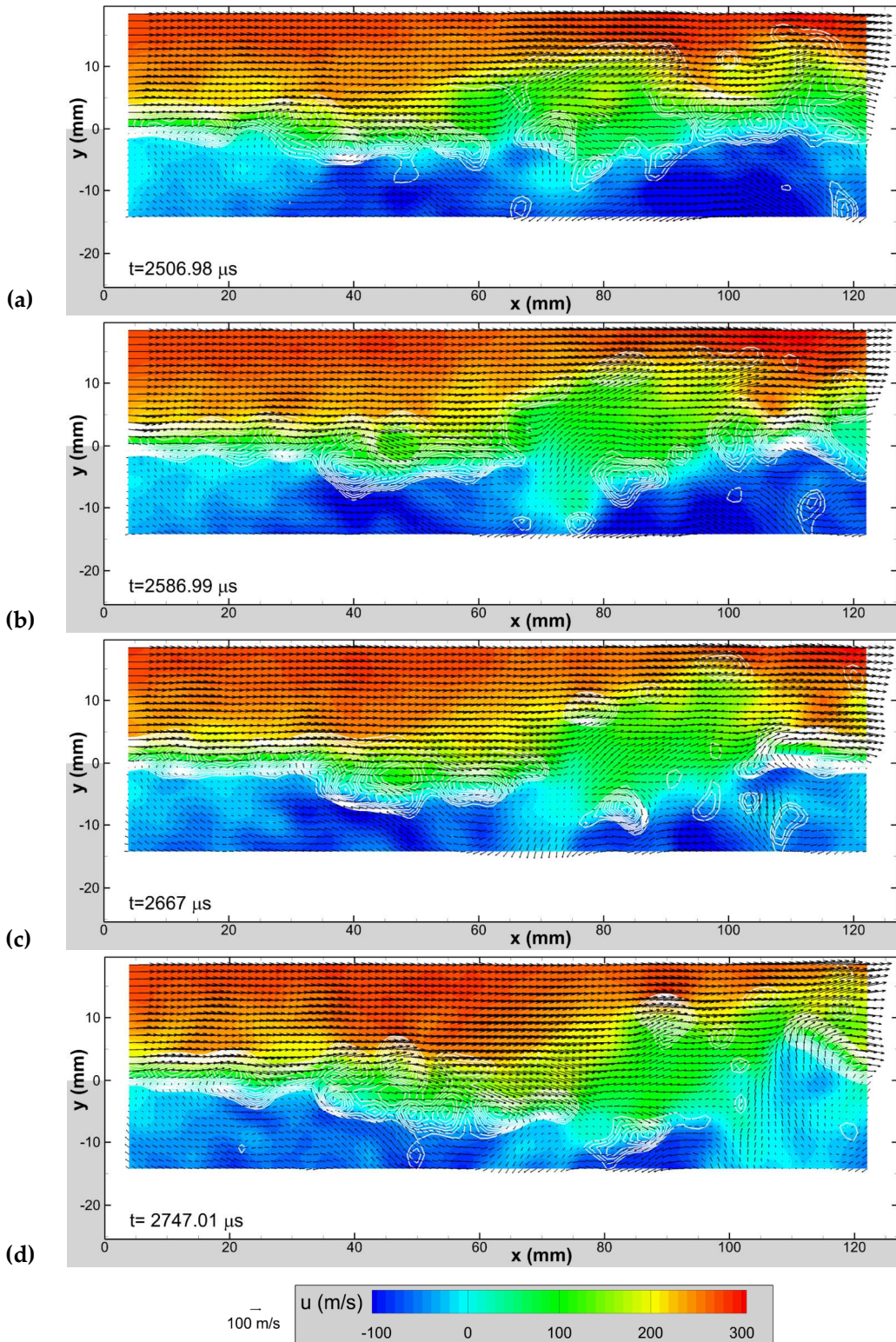


Fig. 5 Sequence of velocity fields extracted from a 10.2 ms burst of 386 velocity fields acquired at 37.5 kHz for flow over a rectangular cavity at Mach 0.8. Vectors show the in-plane velocities superposed on a color contour plot of the streamwise velocity component and white line contours of the vorticity magnitude exceeding a minimum threshold. Initial time is arbitrary from the start of the burst.

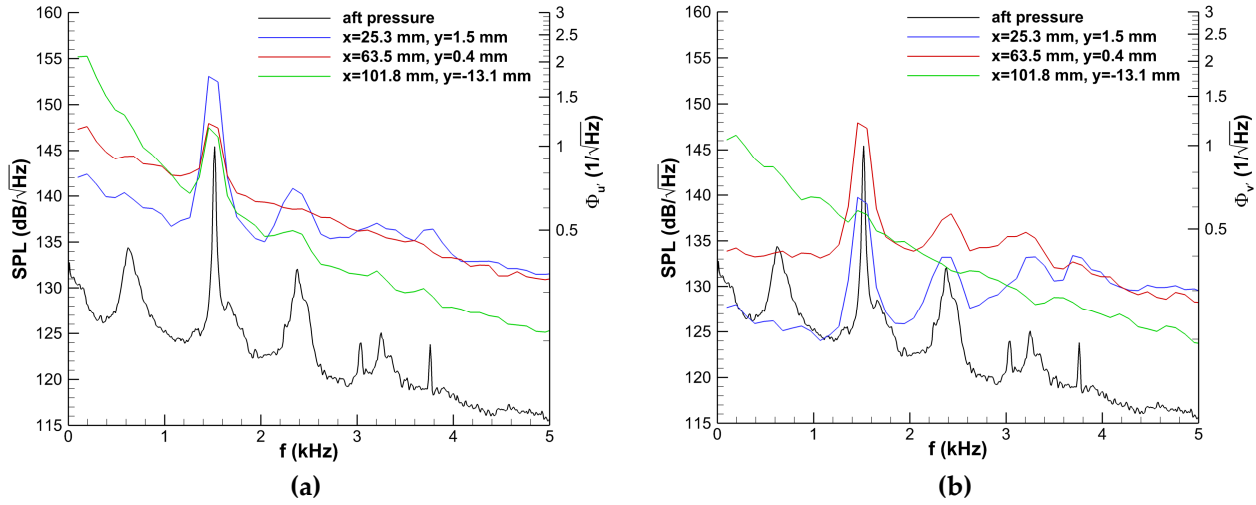


Fig. 6 Power spectra of velocity fluctuations compared to the spectra of pressure fluctuations from a sensor in the aft cavity wall. Three velocity locations are shown: upstream in the shear layer ($x=25.3$ mm, $y=1.5$ mm), mid-length in the shear layer ($x=63.5$ mm, $y=0.4$ mm), and in the recirculation region ($x=101.8$ mm, $y=-13.1$ mm). (a) Streamwise component; (b) Vertical component.

structure that induces a strong event at the aft end of the cavity. The instantaneous structure of the flow within the cavity may not well reflect the mean shear layer and recirculation region characteristic of cavity flows.

PSD's were produced from the 280 bursts similar to Fig. 5 and are given in Fig. 6, where Fig. 6a shows the streamwise component and Fig. 6b the vertical component. Also presented in Fig. 6 is a PSD of the pressure fluctuations recorded by a high-frequency pressure sensor (Kulite XCQ-062) installed in the aft cavity wall at $y = 10.7$ mm on the centerline and sampled at 200 kHz. Three points in the velocity field were selected to represent different gross flowfield features. One was placed upstream in the shear layer at $x = 25.3$ mm, $y = 1.5$ mm and another was placed in the middle of the shear layer at $x = 63.5$ mm, $y = 0.4$ mm. The third point is located within the recirculation region near the aft end of the cavity, $x = 101.8$ mm, $y = -13.1$ mm. Pressure and velocity spectra are necessarily plotted on separate axes, whose relative scaling is arbitrarily selected to ease comparisons of the resonances.

Four acoustic tones are clearly seen in the pressure spectrum, corresponding to the first four Rossiter tones in the cavity. The velocity peaks are broadened in comparison with the pressure peaks – most apparent for mode 2 – because the velocity PSD's were computed using a frequency resolution of 100 Hz limited by the 10.2 ms burst duration, whereas the much longer record length of the pressure data allowed a resolution of 10 Hz. Most of the pressure peaks are

matched in the velocity spectra in both plots of Fig. 6, but their presence varies depending upon resonance mode and choice of velocity component. Mode 1 is not evident in any of the three velocity points. Mode 2, conversely, is most commonly present. It can be seen for the streamwise component for all three points and in at least two of the points for the vertical component; only the point within the recirculation region in Fig. 6b appears not to show evidence of mode 2, though it may be weakly present. Modes 3 and 4 are observed in the velocity spectra as well but inconsistently depending upon the point and component that is examined. Beresh et al [11] provide a more thorough discussion of the resonances found in the cavity and how their spatial distribution creates the contrasts between velocity and pressure data.

Turbulent fluctuations will also be found in the PSD's but at frequencies exceeding those of the resonances. To identify these turbulent properties, temporal supersampling was once again employed. At the freestream velocity, about 13 vectors will convect past in the time between successive velocity fields; a supersampling factor of 12 was chosen as a round number for convenient data handling. The resulting supersampled PSD's are given in Fig. 7 for both the streamwise and vertical velocity components. Unlike the jet-in-crossflow experiment with its narrow field of view and gradual evolution in the far-field, the turbulence characteristics and the length scales of the cavity flow are strong functions of spatial location. Therefore, velocity spectra were extracted at three representative points, each with different flow characteristics. Previous measurements have confirmed that the turbulence is strongest within the shear layer and continually increases with streamwise distance [28].

Figure 7 includes points extracted in the center of the shear layer near the aft wall where the turbulence intensity is highest ($x = 117$ mm, $y = 0$ mm), in the center of the shear layer at an upstream position where the turbulence intensity is more moderate ($x = 54$ mm, $y = 0$ mm), and at this same upstream point but higher in the shear layer where the local convection velocity is closer to the freestream velocity. The streamwise component is suggestive of a region reasonably tangent to a -1 slope but the range over which it persists is a function of position within the cavity. In Fig. 7a, this regime has an onset at about 3 kHz but begins to roll off shortly beyond 10 kHz for the downstream point. Rolloff is delayed until 30 – 40 kHz when the spectrum is moved to the upstream shear layer. The point in the upper shear layer appears more consistently tangent to the -1 slope for more than a decade to about 50 kHz; the lower amplitude is simply a reflection of lower turbulence levels away from the center of the shear layer. The -1 regime is less evident in the vertical velocity component of Fig. 7b. It is possible that this is a

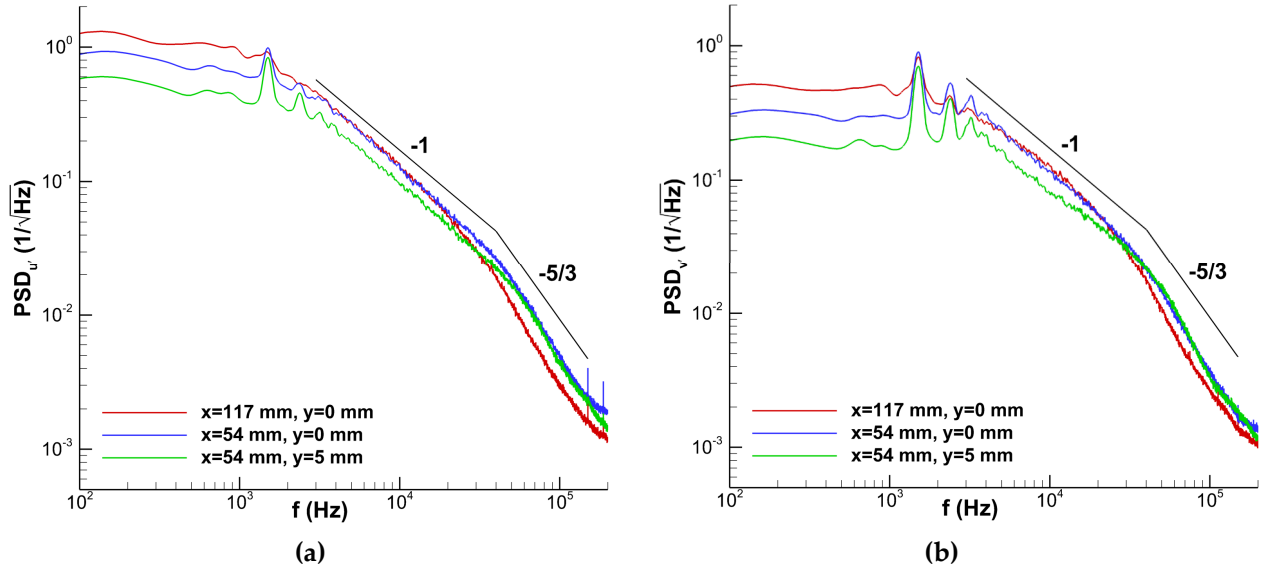


Fig. 7 Supersampled power spectra of velocity fluctuations for the rectangular cavity flow, at positions aft along the shear layer centerline, upstream along the shear layer centerline, and upstream in the outer shear layer, respectively. (a) streamwise component; (b) vertical component.

measurement artifact, as the vertical component experiences contamination from the out-of-plane component due to the downward angle of the cameras as they peer into the cavity.

The frequency at which the slope rolls off from the -1 power law is likely a function of the measurement signal response at each extracted point. The rolloff frequency clearly increases upstream in Fig. 7a. This probably is a reflection of smaller out-of-plane motion at upstream locations, which means that advection is more likely to remain in plane for appropriate use by the supersampling algorithm. Spatial resolution of a vector is a second factor. The frequency rolloff due to spatial resolution is found at smaller frequencies when the local convection velocity is smaller. This, too, is consistent with Fig. 7a; the point higher in the shear layer will possess a higher local convection velocity and indeed it shows a higher frequency rolloff than the lower point.

The -5/3 slope of the inertial subrange is reasonably well matched up to perhaps 150 kHz by the two upstream points in Fig. 7a, but the point farther downstream in the shear layer appears to exhibit a somewhat steeper slope. Again, the data from the vertical component show poorer agreement with the scaling law in Fig. 7b. Frequency response limitations are likely to hinder accurate measurement of the inertial subrange. The only cavity flow experiment known to have

detected the $-5/3$ scaling law of the inertial subrange is Liu and Katz [29] in a low-Reynolds-number water tunnel. Seena and Sung [30] located it in a Direct Numerical Simulation.

To again employ Pope's estimate that the inertial subrange should begin at $1/6$ of the integral length scale, the vorticity thickness of the shear layer was used as a measure of the largest scales of the flow [31]. As the shear layer grows, the vorticity thickness grows as well and therefore the expected frequency corresponding to the inertial subrange shifts to lower values. At the upstream point of $x = 54$ mm, the vorticity thickness predicts an onset at about 80 kHz; as the aft end of the cavity nears and the shear layer thickens, this drops to 40 kHz. Figure 7 suggests that a transition from the -1 regime to the inertial subrange occurs at about 40 kHz for the upstream point at $y = 0$ mm and drops to 10 - 20 kHz farther downstream. The upstream $y = 5$ mm point retains a -1 power-law dependency until 50 kHz. In each case, the -1 regime appears to terminate earlier than Pope's prediction. This may be a consequence of measurement limitations as discussed, or possibly the vorticity thickness underestimates the integral length scale.

The limitations in the supersampling technique may account for the weaker consistency with turbulence scaling laws in comparison to the jet-in-crossflow experiment. Out-of-plane motion is greater in this case, reaching a peak turbulence intensity in this component of 0.3; therefore, the planar measurement might not accurately track the advection of turbulent fluctuations. Secondly, it is not dominated by convection as the far-field jet-in-crossflow measurements were. This means the spatial resolution of a single vector becomes a limitation at lower frequencies since the local convection velocity typically will be smaller. In fact, the estimated limit is about 60 kHz in the center of the shear layer and approximately 100 kHz near its outer edge; this may account for the superior agreement with the turbulent decay power laws for the point farthest from the cavity in Fig. 7. Spectra obtained farther from the cavity will have superior frequency response due to the higher mean convection velocity and indeed this shows the best agreement with the -1 and $-5/3$ power laws (in Fig. 7a; the vertical component in Fig. 7b will experience some out-of-plane contamination). This suggests that if the measurement contains minimal out-of-plane motion and is not limited by spatial resolution, as is the case upstream and at the outer edge of the shear layer, both of these turbulent scaling laws will emerge through supersampling.

3.3 Cylinder Wake

The transient wake growth downstream of the cylinder in the shock tube is shown in Fig. 8, where vorticity contours are plotted along with overlaid velocity vectors. The shock-induced velocity, U_2 , has been measured as 175 m/s, yielding a Reynolds number based on cylinder

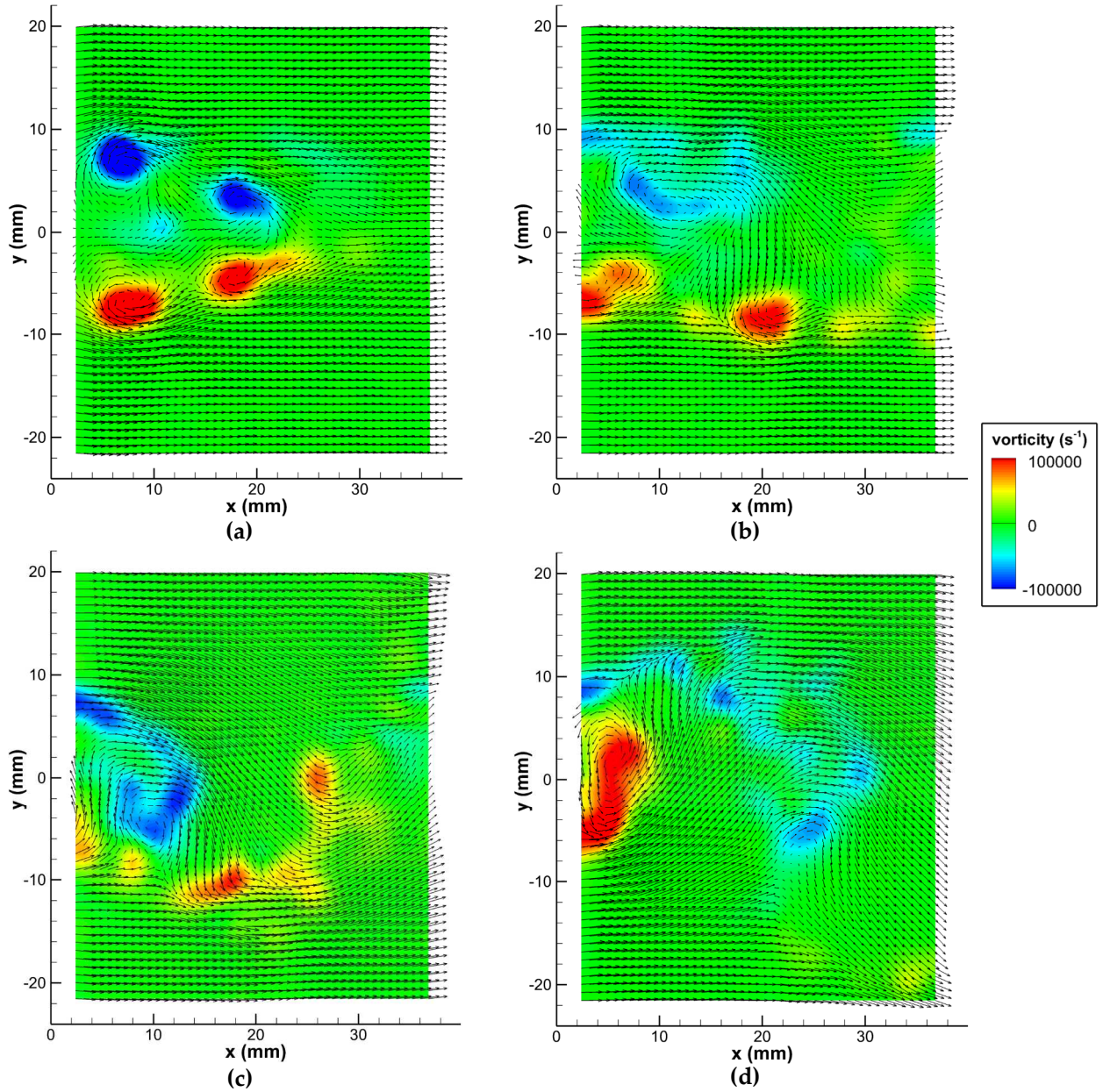


Fig. 8 Sample velocity fields of the transient onset of vortex shedding in the wake of a cylinder, extracted from an approximately 6 ms sequence at 50 kHz. Initial time is set to shock passage over the cylinder. (a) $t = 436 \mu\text{s}$; (b) $t = 776 \mu\text{s}$; (c) $t = 1916 \mu\text{s}$; (d) $t = 2076 \mu\text{s}$.

diameter of about 1.8×10^5 . The coordinate origin in the figure is defined to be at the trailing edge of the cylinder.

Figure 8 shows four snapshots exhibiting the transient onset of vortex shedding. In Fig. 8a, occurring $436 \mu\text{s}$ after the shock passes over the cylinder, the first two pairs of vortices that are shed from the cylinder can be seen. Unlike a von Kármán vortex street, these vortices are

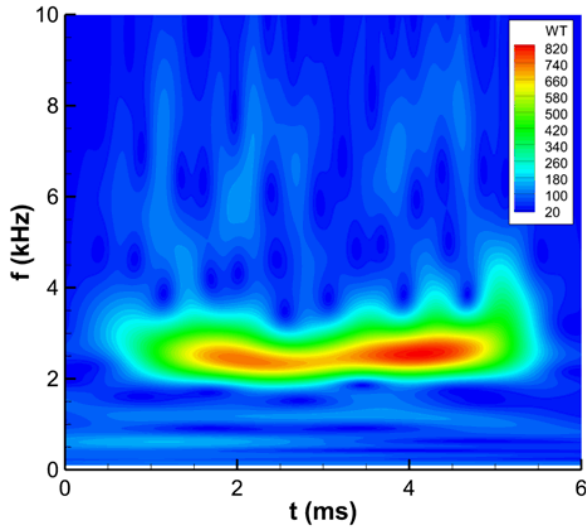


Fig. 9: Wavelet transform of the vertical velocity component in the wake of the cylinder at $x = 14$ mm, $y = 0$, showing the transient nature of the frequency spectrum.

oriented symmetrically. As time progresses, subsequent pairs of shed vortices shift to a more familiar asymmetric arrangement, which can be seen in Fig. 8b at 776 μ s after shock passage. At later times, the wake is beginning to oscillate in a periodic fashion consistent with von Kármán vortex shedding and this can be seen in Figs. 8c and 8d. The shock tube experiments of Asher and Dosanjh [32] also showed two symmetric vortex pairs to form prior to the wake becoming asymmetric. The von Kármán street continues until the arrival of the reflected shock at about $t = 5.2$ ms (not shown).

Since the transient onset of vortex shedding begins symmetric and then shifts to become asymmetric, the frequency content of the flow can be expected to be a function of time. Thus, spectral analysis of the data needs to be considered not using PSD's as in the two wind tunnel examples, but rather by employing joint time-frequency analysis using wavelet transforms. The wavelet transform was computed using a Mathworks (Matlab) script and a Morelet mother wavelet.

The time evolution of the velocity fluctuations within the wake is shown in Fig. 9, where the amplitude of the wavelet transform is given as a function of time and frequency. The analysis shows the vertical velocity component at the location of $x = 14$ mm and $y = 0$ mm. The wavelet transform magnitude begins to increase in amplitude at about 0.5 ms and rises to a peak shortly after 1.5 ms. This coincides with the establishment of asymmetric vortex shedding, which the wavelet transform shows to occur at a frequency of 2430 Hz. This frequency corresponds to a Strouhal number based on cylinder diameter ($St = fd/U_2$) of 0.19, a value consistent with the

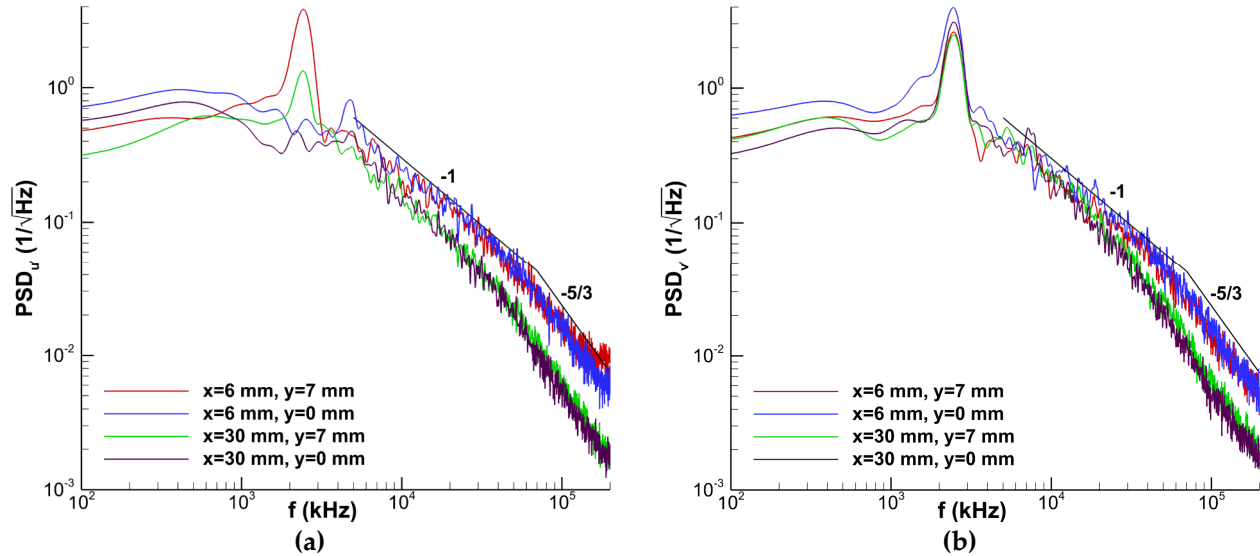


Fig. 10: Supersampled power spectra of velocity fluctuations for the cylinder wake flow at varying position. (a) streamwise component; (b) vertical component.

literature at the current Re_d [33]. The vortex shedding then maintains an approximately steady state until the arrival of the reflected shock terminates the flow at about 5 ms.

Supersampling was again employed with a factor of 12 and the resulting spectra are shown in Fig. 10 for both streamwise and vertical velocity components. These data were obtained only during the steady portion of the flow, from 1.5 ms to 5.2 ms. Four points in the flow are given. The two points at $x = 6$ mm are in the very near wake of the cylinder with $y = 0$ mm centered behind it and $y = 7$ mm aligned with the radius of the cylinder near the point from which vortices are shed. The same two vertical positions are interrogated again near the downstream extent of the field of view. Points must be chosen suitably distant from the edges of the velocity fields such that the algorithm will not extrapolate data that convect beyond the bounds of the field of view. The data are noisier than for the two wind tunnel cases because only 15 shock tube runs were available to construct the spectra.

The peak at about 2500 Hz corresponds to the vortex shedding frequency identified in the wavelet transform of Fig. 9. At frequencies only a little beyond this, an apparent power law slope dependence of -1 again emerges, extending until approximately 50 – 60 kHz. Beginning about 70 kHz, the slope descends to match a -5/3 dependence to suggest the presence of an inertial subrange. Vector spatial resolution corresponds to a frequency response of about 120 kHz and therefore should not limit detection of the inertial subrange at the identified frequencies. For both regions, the data in the very near wake better match the theoretical slopes

than the two data points acquired farther downstream. At these more distant points, the large vortices shed from each side of the cylinder may interact with each other similarly to the large-scale vortices in the low-Reynolds-number jet of Scarano and Moore [6], which they suggest is responsible for a breakdown in the advected frozen turbulence assumption used by the supersampling algorithm. Therefore, it is plausible that the spectra found at upstream points are more reliable than those at downstream points, which may explain their better agreement with the -1 and -5/3 power laws. Figures 8c and 8d, as well as other instances from the full pulse-burst PIV movie, show that the vortices shed from the cylinder are already breaking down into smaller eddies by the time they reach $x = 6$ mm and therefore represent a range of structure sizes consistent with the energy-containing eddies that would comprise the -1 power law region.

The inertial subrange has been measured previously in the spectra of the near wake of a cylinder by Ong and Wallace [34] and much farther downstream by Uberoi and Freymuth [35]. Large-eddy simulations also have reproduced the inertial subrange [36]. However, no known turbulent vortex-shedding experiments have suggested the existence of a -1 power law at the scale of energetic eddies.

3.4 Validation

The application of temporal supersampling to three different free shear flows measured using pulse-burst PIV have revealed power-law dependencies for turbulent decay. The well-known inertial subrange and its -5/3 slope is observed at large frequencies, but unexpectedly also a -1 slope emerges at mid-range frequencies consistent with the regime of energy-containing turbulent eddies. Although this latter regime occurs at frequencies that ought to be well removed from the frequency limitations of supersampling, a validation of the technique is warranted.

To accomplish this, the pulse-burst PIV configuration was altered to acquire data at much higher repetition rates. The laser was increased to a frequency of 400 kHz and set to generate single pulses rather than pulse pairs, creating a time between successive pulses of 2.5 μ s. Under these conditions, the laser produced 3 mJ of 532 nm light per pulse for a burst duration of 10.2 ms. The SA-Z cameras can operate at this high frequency only if they are windowed down to a small array of only 128×120 pixels, giving rise to the facetious moniker of “postage-stamp PIV.” The laser sheet was narrowed to a slender width to concentrate the available energy in the small field of view. These data cannot provide much spatial coverage but their intent is to produce spectral content at very high frequency without the assumptions inherent in supersampling.

Postage-stamp PIV measurements have been conducted on the jet in crossflow and the cavity flow. The cameras were configured to retain the same spatial resolution as the supersampled measurements so as to replicate any modulation due to the finite interrogation window size. The different time between laser pulses is not sufficient to be the dominant limitation in the frequency response of the measurements. By replicating the spatial resolution, the postage-stamp PIV data can be compared to the supersampled data and test the assumption of advected frozen turbulence that underlies the supersampling technique.

Data acquisition was nearing completion as this paper was written and could not be analyzed in sufficient time for inclusion. A future publication will address the validation of supersampling and provide confirmation of the power-law scaling revealed in the present high-speed flowfields.

4. Conclusions

Time-resolved PIV has been accomplished in high-speed flows using a pulse-burst laser. The frequency response of the resulting data can be increased substantially by employing temporal supersampling to convert spatial information into temporal information, employing Taylor's frozen turbulence hypothesis to move velocity data along local streamlines. This technique has been applied to three high-speed flows: a supersonic jet exhausting into a transonic crossflow, a transonic flow over a rectangular cavity, and a shock-induced transient onset to cylinder vortex shedding.

Power spectra reduced from the supersampled PIV data are valid until about 150 kHz where the noise floor is reached. The spectra consistently reveal two regions exhibiting slopes with a constant power-law dependence describing the turbulent decay. One is the well-known inertial subrange with a slope of $-5/3$ at high frequencies. The other displays a -1 power-law dependence for as much as a decade of mid-range frequencies lying between the inertial subrange and the integral length scale. The evidence for the -1 power law is most convincing in the jet-in-crossflow experiment, for which the flow is dominated by in-plane convection and the vector spatial resolution does not impose an additional frequency constraint. The transonic cavity flow covers a larger field of view and spatial resolution limits may attenuate the spectra at frequencies within the reach of supersampling. It also has strong out-of-plane turbulent motion that cannot be tracked for a planar measurement. However, points in the flowfield that are least likely to be subject to limited spatial resolution or out-of-plane motion exhibit the strongest agreement with the -1 and $-5/3$ power laws. The cylinder wake data also appear to show the -1

regime and the inertial subrange in the near-wake, but farther downstream the frozen-turbulence assumption may deteriorate as large-scale vortices interact with one another in the von Kármán vortex street.

Additional pulse-burst PIV experiments are underway at very high frequencies to validate the supersampling technique in the present high-speed flows. These will be reported in a future publication.

References

- [1] Wernet, M., "Temporally Resolved PIV for Space-Time Correlations in Both Cold and Hot Jet Flows," *Measurement Science and Technology*, Vol. 18, No. 5, 2007, pp. 1387-1403.
- [2] Brock, B., Haynes, R. H., Thurow, B. S., Lyons, G., and Murray, N. E., "An Examination of MHz Rate PIV in a Heated Supersonic Jet," *AIAA Paper 2014-1102*, January 2014.
- [3] Miller, J. D., Michael, J. B., Slipchenko, M. N., Roy, S., Meyer, T. R., and Gord, J. R., "Simultaneous High-Speed Planar Imaging of Mixture Fraction and Velocity using a Burst-Mode Laser," *Applied Physics B*, Vol. 113, 2013, pp. 93-97.
- [4] Miller, J. D., Gord, J. R., Meyer, T. R., Slipchenko, M. N., Mance, J. G., and Roy, S., "Development of a Diode-Pumped, 100-ms Quasi-Continuous Burst-Mode Laser for High-Speed Combustion Diagnostics," *AIAA Paper 2014-2524*, June 2014.
- [5] Beresh, S. J., Kearney, S. P., Wagner, J. L., Guildenbecher, D. R., Henfling, J. F., Spillers, R. W., Pruett, B. O. M., Jiang, N., Slipchenko, M., Mance, J., and Roy, S., "Pulse-Burst PIV in a High-Speed Wind Tunnel," *Measurement Science and Technology*, Vol. 26, No. 9, 2015, pp. 095305..
- [6] Scarano, F., and Moore, P., "An Advection-Based Model to Increase the Temporal Resolution of PIV Time Series," *Experiments in Fluids*, Vol. 52, No. 4, 2012, pp. 919-933.
- [7] Del Alamo, J. C., and Jimenez, J., "Estimation of Turbulent Convection Velocities and Corrections to Taylor's Approximation," *Journal of Fluid Mechanics*, Vol. 640, 2009, pp. 5-26.
- [8] Schneiders, J. F. G., Dwight, R. P., and Scarano, F., "Time-Supersampling of 3D-PIV Measurements with Vortex-in-Cell Simulation," *Experiments in Fluids*, Vol. 55, No. 3, 2014, pp. 1692.

[9] Schreyer, A.-M., Larchevêque, L., and Dupont, P., "Method for Spectra Estimation from High-Speed Experimental Data," *AIAA Journal*, Vol. 54, No. 2, 2016, pp. 557-568.

[10] Beresh, S. J., Wagner, J. L., Henfling, J. F., Spillers, R. W., and Pruett, B. O. M., "Turbulent Eddies in a Compressible Jet in Crossflow Measured using Pulse-Burst Particle Image Velocimetry," *Physics of Fluids*, Vol. 28, No. 2, 2016, pp. 025102.

[11] Beresh, S. J., Wagner, J. L., DeMauro, E. P., Henfling, J. F., and Spillers, R. W., "Resonance Characteristics of Transonic Flow over a Rectangular Cavity using Pulse-Burst PIV," *AIAA Paper 2016-1344*, San Diego, CA, January 2016.

[12] Wagner, J. L., Beresh, S. J., Casper, K. M., DeMauro, E. P., Arunajatesan, S., Henfling, J. F., and Spillers, R. W., "Relationship between Transonic Cavity Tones and Flowfield Dynamics using Pulse-Burst PIV," *AIAA Paper 2016-1345*, San Diego, CA, January 2016.

[13] Wagner, J. L., Beresh, S. J., DeMauro, E. P., Casper, K. M., Gildenbecher, D. R., Pruett, B., and Farias, P., "Pulse-Burst PIV Measurements of Transient Phenomena in a Shock Tube," *AIAA Paper 2016-0791*, San Diego, CA, January 2016.

[14] Wagner, J. L., Casper, K. M., Beresh, S. J., Henfling, J. F., Spillers, R. W., and Pruett, B. O. M., "Mitigation of Wind Tunnel Wall Interactions in Subsonic Cavity Flows," *Experiments in Fluids*, Vol. 56, No. 3, 2015, pp. 59.

[15] Beresh, S. J., Wagner, J. L., and Pruett, B. O. M., "Particle Image Velocimetry of a Three-Dimensional Supersonic Cavity Flow," *AIAA Paper 2012-0030*, January 2012.

[16] Wagner, J. L., Beresh, S. J., Kearney, S. P., Trott, W. M., Castaneda, J. N., Bruett, B. O., and Baer, M. R., "A Multiphase Shock Tube for Shock Wave Interactions with Dense Particle Fields," *Experiments in Fluids*, Vol. 52, No. 6, 2012, pp. 1507-1517.

[17] Pope, S. B., *Turbulent Flows* (Cambridge University Press, 2000), pp. 228-242.

[18] Kawai, S., and Lele, S. K., "Large-Eddy Simulation of Jet Mixing in Supersonic Crossflows," *AIAA Journal*, Vol. 48, No. 9, 2010, pp. 2063-2083.

[19] Bull, M. K., "Wall-Pressure Fluctuations Beneath Turbulent Boundary Layers: Some Reflections on Forty Years of Research," *Journal of Sound and Vibration*, Vol. 190, No. 3, 1996, pp. 299-315.

[20] Perry, A. E., Henbest, S., and Chong, M. S., "A Theoretical and Experimental Study of Wall Turbulence," *Journal of Fluid Mechanics*, Vol. 165, 1986, pp. 163-199.

[21] Nickels, T. B., Marusic, I., Hafez, S., and Chong, M. S., "Evidence of the $k^{1/4}$ - 1 Law in a High-Reynolds-Number Turbulent Boundary Layer," *Physical Review Letters*, Vol. 95, No. 7, 2005, pp. 074501.

[22] Rosenberg, B. J., Hultmark, M., Vallikivi, M., Bailey, S. C. C., and Smits, A. J., "Turbulence Spectra in Smooth- and Rough-Wall Pipe Flow at Extreme Reynolds Numbers," *Journal of Fluid Mechanics*, Vol. 731, 2013, pp. 46-63.

[23] Nickels, T. B., Marusic, I., Hafez, S., Hutchins, N., and Chong, M. S., "Some Predictions of the Attached Eddy Model for a High Reynolds Number Boundary Layer," *Philosophical Transactions of the Royal Society A*, Vol. 365, No. 1852, 2007, pp. 807-822.

[24] Stanislas, M., Okamoto, K., Kähler, C. J., Westerweel, J., and Scarano, F., "Main Results of the Third International PIV Challenge," *Experiments in Fluids*, Vol. 45, No. 1, 2008, pp. 27-71.

[25] Nogueira, J., Lecuona, A., and Rodriguez, P. A., "Limits on the Resolution of Correlation PIV Iterative Methods. Fundamentals," *Experiments in Fluids*, Vol. 39, No. 2, 2005, pp. 305-313.

[26] Scarano, F., "Iterative Image Deformation Methods in PIV," *Measurement Science and Technology*, Vol. 13, No. 1, 2002, pp. R1-R19.

[27] Beresh, S. J., Henfling, J. F., Erven, R. J., and Spillers, R. W., "Turbulent Characteristics of a Transverse Supersonic Jet in a Subsonic Compressible Crossflow," *AIAA Journal*, Vol. 43, No. 11, 2005, pp. 2385-2394.

[28] Beresh, S. J., Wagner, J. L., Henfling, J. F., Spillers, R. W., and Pruett, B. O. M., "Width Effects in Transonic Flow over a Rectangular Cavity," *AIAA Journal*, Vol. 53, No 12, 2015, pp. 3831-3834.

[29] Liu, X., and Katz, J., "Vortex-Corner Interactions in a Cavity Shear Layer Elucidated by Time-Resolved Measurements of the Pressure Field," *Journal of Fluid Mechanics*, Vol. 728, 2013, pp. 417-457.

[30] Seena, A., and Sung, H. J., "Dynamic Mode Decomposition of Turbulent Cavity Flows for Self-Sustained Oscillations," *International Journal of Heat and Fluid Flow*, Vol. 32, No. 6, 2011, pp. 1098-1110.

[31] Beresh, S. J., Wagner, J. L., and Casper, K. M., "Compressibility Effects in the Shear Layer over a Rectangular Cavity," to be presented at the AIAA Aviation Forum, Washington DC, June 2016.

[32] Asher, J. A., and Dosanjh, D. S., "An Experimental Investigation of Formation and Flow Characteristics of an Impulsively Generated Vortex Street," *Journal of Basic Engineering*, Vol. 90, No. 4, 1968, pp. 596.

[33] Roshko, A., "Experiments on the Flow Past a Circular Cylinder at Very High Reynolds Number" *Journal of Fluid Mechanics*, Vol. 10, No. 3, 1961, pp. 345-346.

[34] Ong, L., and Wallace, J., "The velocity Field of the Turbulent Very Near Wake of a Circular Cylinder," *Experiments in Fluids*, Vol. 20, No. 6, 1996, pp. 441-453.

[35] Uberoi, M. S., and Freymuth, P., "Spectra of Turbulence in Wakes Behaind Circular Cylinders," *Physics of Fluids*, Vol. 12, No. 7, 1969, pp. 1359-1363.

[36] Ma, X., Karamanos, G.-S., and Karniadakis, G. E., "Dynamics and Low-Dimensionality of a Turbulent Near Wake," *Journal of Fluid Mechanics*, Vol. 410, 2000, pp. 29-65.